Multivariable Control and Optimization of a Compact 6-DOF Precision Positioner With Hybrid $\mathcal{H}_2/\mathcal{H}_\infty$ and Digital Filtering

Jose Christian Silva-Rivas and Won-jong Kim, *Senior Member, IEEE*

***Abstract*— In this paper, we present multivariable controller design and implementation of a high-precision 6-DOF magnetically levitated (maglev) positioner. To achieve high-precision positioning, two discrete-time integrator-augmented controllers based on the linear quadratic Gaussian multivariable control are applied. A novel discrete hybrid $\mathcal{H}_2/\mathcal{H}_\infty$ filter is used as the observer to obtain the optimal estimates of position and orientation, as well as additional estimates of linear and angular velocities for all six axes. The positioner has a single moving part that carries three 3-phase permanent-magnet linear-levitation-motor armatures. The positioner moves over a Halbach magnet matrix using three sets of two-axis Hall-effect sensors to measure the planar motion and three laser distance sensors for the vertical motion. The Hall-effect sensor signals are found to generate a considerable amount of noise and are centered at 50 Hz. A second-order digital notch filter is implemented to optimize the sensor readings and attenuate the noise. Experimental results show a position resolution, which is the smallest noticeable step of 1.5 μm with a position noise of 0.545 μm rms in the *x*- and *y*-directions, and a position resolution of 110 nm with a position noise of 49.3 nm rms in the *z*-direction.**

***Index Terms*— Compact positioner, digital filtering, hybrid $\mathcal{H}_2/\mathcal{H}_\infty$ filtering, integrator-augmented linear quadratic (LQ), multivariable control, precision motion control.**

I. Introduction

In THE modern semiconductor manufacturing industry, high-precision motion control is a key component for wafer steppers, surface profilometers, and scanned-probe microscopes. In the high-accuracy positioning and sophisticated photolithographic process, wafer steppers are used to manufacture integrated circuits via fully automated control generating step-and-repeat motions [1]. An optical source sheds a deep-ultraviolet beam through a photomask onto each die site on the wafer [2]. The wafer stage is required to move the wafer in all six directions with minimum errors and should have high resolution and accuracy. This wafer stepper stage in semiconductor manufacturing is the main application of the work presented in this paper.

Manuscript received December 9, 2011; revised July 9, 2012; accepted August 17, 2012. Manuscript received in final form August 21, 2012. Date of publication October 5, 2012; date of current version August 12, 2013. Recommended by Associate Editor Q. Wang.

The authors are with the Department of Mechanical Engineering, Texas A&M University, College Station, TX 77845 USA (e-mail: jcs829@neo.tamu.edu; wjkim@tamu.edu).

Color versions of one or more of the figures in this paper are available online at http://ieeexplore.ieee.org.

Digital Object Identifier 10.1109/TCST.2012.2215035

A planar motor can be used as an actuator for a precision-positioning stage. The advantage of a planar motor is that it can generate high-precision multidimensional motions with a large travel range. By their working principles, most of the planar motors can be classified into Sawyer motors, synchronous permanent-magnet planar motors (SPMPMs), and induction planar motors [3]. The induction planar motor is a two-axis linear induction motor, and this type of planar motors are still in their development stage [4]. The Sawyer motor is a planar stepper motor, which is made by conceptually superimposing two orthogonal variable reluctance motors. Some Sawyer motors have already been commercialized [5], [6] and exhibit a positioning repeatability on the order of 5 μm. Sawyer motors are susceptible to large cogging and loss of steps [7]. As their motion is tightly constrained to a plane, Sawyer motors cannot provide local leveling without using other fine motion actuators.

The compact 6-DOF precision positioner shown in Fig. 1 was developed by Yu [8] and has three 3-phase SPMPMs. The concentrated-field permanent-magnet matrix beneath the mirror-finished aluminum plate was made by superimposing two Halbach magnet arrays [9], [10]. This magnet matrix of $304.8 \times 304.8 \times 12.7$ mm serves as the stator. By changing the magnitude and direction of their phase currents, the three planar motors can generate both levitation and driving forces. The detailed working principle including the electromagnetic analysis was presented in [11].

The most significant feature of the stage is that the single moving part, namely the platen, currently levitated by the three aerostatic bearings, can generate all 6-DOF fine and coarse motions. Any 6-DOF motions can be generated by a combination of the six force components of the platen. This mechanically noncontact machine structure does not need lubricants nor does it produce wear particles. Therefore, it is suited for clean-room environment. Superimposing multiple linear motors as one actuator reduces the footprint. Compared to traditional positioners, the single moving frame can have high natural frequencies. The simple design eliminates complicated components and reduces the manufacturing cost with high reliability [10], [12]. The frame of the platen is made of Delrin with a mass density of 1.54 g/cm^3 in order to reduce the total mass. The triangular design is chosen for simplicity. The total mass of the moving platen is 1.52 kg. The travel ranges are 220 mm in the x-direction and 200 mm in the y-direction. The rotational travel range of 12° was achieved around the

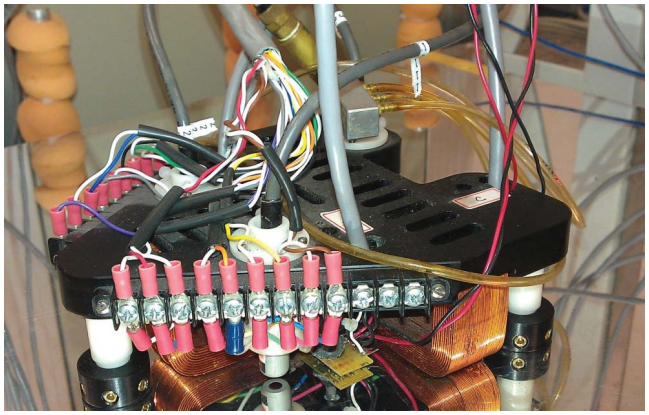

Fig. 1. Photograph of the 6-DOF precision positioner.

z-axis [8], [13], which is perpendicular to the top surface of the magnet matrix.

The position resolution of the positioner is around 16 μm peak to peak [8], [13]. However, for the semiconductor industry, one needs to get the positioning resolution as small as possible, and this can be achieved by optimizing the Hall-effect sensor signals. In [14], a method of combining $\mathcal{H}_2$ and $\mathcal{H}_\infty$ filters into a hybrid filter was proposed, aiming to make the most of the advantages that each individual filter offers to obtain better estimates and enhance stability. Simulations were conducted in [15] by applying such an approach for global positioning system satellite signals to correct a solution from an inertial navigation system, but no experimental result was recorded to validate the advantages of the hybrid filter.

In this paper, we implement this $\mathcal{H}_2/\mathcal{H}_\infty$ hybrid filter and use its outputs for the multivariable control of the positioner. For the multi-input multi-output (MIMO) controllers, a linear quadratic Gaussian (LQG) approach is used. The LQG methodology usually refers to the combination of a linear quadratic (LQ) regulator and a Kalman filter to provide the full-state feedback. In this paper, an $\mathcal{H}_2/\mathcal{H}_\infty$ hybrid filter is implemented to estimate the states.

This paper consists of six sections. In Section II, the dynamic analysis and system modeling are briefly described. In Section III, the multivariable controller design and the discrete hybrid $\mathcal{H}_2/\mathcal{H}_\infty$ filter acting as the observer are discussed. Section IV contains the analysis done on the Hall-effect sensors in order to reject the sensor signals' noise. From this analysis, a step-by-step procedure on the design of a second-order digital notch filter to optimize the sensor signal is presented. Section V presents the experimental results to demonstrate the effectiveness of both the designed MIMO controllers and the hybrid $\mathcal{H}_2/\mathcal{H}_\infty$ filter, as well as the comparisons with the results obtained in the previous work. Section VI presents the conclusions on the experimental results and discusses the performances of both the multivariable controllers and the hybrid $\mathcal{H}_2/\mathcal{H}_\infty$ filter.

II. Modeling

Fig. 2 illustrates the free-body diagram of the positioner, the convention for the coordinate system, and the directions of the six independent force components generated by the three

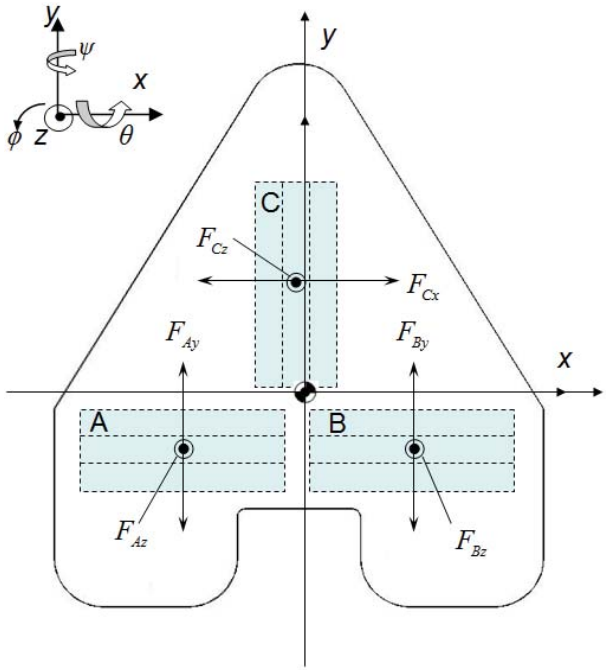

Fig. 2. Coordinate system and free-body diagram of the positioner.

levitation motors. The windings of the three 3-phase planar motors A, B, and C are attached on the bottom surface of the platen (as shown in Fig. 2). Motors A and B are responsible for generating the magnetic forces in the y-direction. Motor C generates the magnetic force in the x-direction. All the three motors can generate z-direction forces independently [10]. Thus the controller can make the positioner generate translation in the x-, y-, and z-axes as well as rotational motions around these axes.

According to the inverse Blondel–Park transformation, the relationship between the peak currents and the phase currents i_A, i_B, and i_C of each winding is shown in [16] and [17]. The relation between the phase currents and the mechanical subsystem is linked by the magnetic force (1), which is derived by the electromagnetic analysis [10], [18]

$$\begin{bmatrix} f_y \\ f_z \end{bmatrix} = \frac{1}{2}\mu_0 M_0 \eta_0 N_m G e^{-\gamma_1 z_0} \begin{bmatrix} \cos\gamma_1 y_0 & \sin\gamma_1 y_0 \\ -\sin\gamma_1 y_0 & \cos\gamma_1 y_0 \end{bmatrix} \times \begin{bmatrix} \frac{2}{3} & -\frac{1}{3} & -\frac{1}{3} \\ 0 & \frac{1}{\sqrt{3}} & -\frac{1}{\sqrt{3}} \end{bmatrix} \begin{bmatrix} i_A \\ i_B \\ i_C \end{bmatrix} \quad (1)$$

where f_y and f_z are the y-directed and z-directed magnetic forces, respectively, and i_A, i_B, and i_C are the input phase currents. The constant G contains the effects of the motor geometry and is 1.072×10^{-5} m^3. The variable y_0 represents a relative displacement in motors A and B. The parameters have the following values: magnetic remanence $\mu_0 M_0 = 0.71$T, effective spatial period $N_m = 2$, pitch $l = 50.98$ mm, absolute value of the fundamental wave number $\gamma_1 = 2\pi/l = 123.25$ m^{-1}, nominal motor air gap $z_0 = 2.3$ mm, winding thickness $\Gamma = l/5 = 10.16$ mm, and magnet array thickness $\Delta = l/4 = 12.7$ mm.

Equation (1) presents only the force components for one planar motor in the y-direction. Motor C has a similar force

equation in f_x and f_z with the corresponding displacement variable x due to the symmetry of the concentrated-field magnet matrix. Since the stage is levitated by air bearings, there is no mechanical friction. Thus, the dynamics of the stage in the horizontal mode can be represented as a pure-mass model as follows:

$$M\frac{d^2x}{dt^2} = f_x, \quad M\frac{d^2y}{dt^2} = f_y \tag{2}$$

$$I_{zz}\frac{d^2\phi}{dt^2} = \tau_z. \tag{3}$$

Similarly for the vertical mode, except that due to the stage being levitated by the aerostatic bearings, the system is modeled as a spring-mass system. The three aerostatic bearings are modeled as three springs with spring constants of K_z, K_θ, and K_ψ. The three springs support the platen in parallel connection. Thus the dynamics of the stage in the vertical mode can be represented as follows:

$$M\frac{d^2z}{dt^2} = f_z - K_z z \tag{4}$$

$$I_{xx}\frac{d^2\theta}{dt^2} = \tau_\theta - K_\theta\theta, \quad I_{yy}\frac{d^2\psi}{dt^2} = \tau_\psi - K_\psi\psi. \tag{5}$$

By Hooke's law, the spring constant in the z-direction K_z was experimentally determined to be 620 N/m. The torsional spring constants about the x- and y-axes K_θ and K_ψ were found to be 65 and 87 N·m/rad, respectively. The principal moments of inertia I_{xx}, I_{yy}, and I_{zz} about the x-, y- and z-axes are 0.0037, 0.0019, and 0.0022 kg·m^2, respectively. F_z is the vertical force and τ_θ and τ_ψ are the torques about the x- and y-axes generated by the planar motors. However, if (1) is substituted into the right-hand sides of (2)–(5), we get nonlinear dynamic models due to the exponential and sinusoidal spatial dependences in (1). Then, a DQ decomposition method is applied to the system as follows [18]:

$$\begin{bmatrix} i_Q \\ i_D \end{bmatrix} = \begin{bmatrix} \cos\gamma_1 y_0 & \sin\gamma_1 y_0 \\ -\sin\gamma_1 y_0 & \cos\gamma_1 y_0 \end{bmatrix} \begin{bmatrix} \frac{2}{3} & -\frac{1}{3} & -\frac{1}{3} \\ 0 & \frac{1}{\sqrt{3}} & -\frac{1}{\sqrt{3}} \end{bmatrix} \begin{bmatrix} i_A \\ i_B \\ i_C \end{bmatrix}. \tag{6}$$

The vertical motion is affected by the direct-component current i_D and the horizontal driving forces are affected by the quadrature-component current i_Q [19]. Through the DQ decomposition, the nonlinear term can be eliminated. The detailed electromagnetic analysis is given in [20]. Finally, the force (1) can now be represented as the following linear equation:

$$\begin{bmatrix} f_y \\ f_z \end{bmatrix} = \frac{1}{2}\mu_0 M_0 \eta_0 N_m G e^{-\gamma_1 z_0} \begin{bmatrix} i_Q \\ i_D \end{bmatrix}. \tag{7}$$

Three Hall-effect sensors and three laser distance sensors are attached to the moving platen and are used to measure the horizontal and vertical positions of the stage. The horizontal position of the moving platen in the coordinate system fixed to the magnet matrix is determined by the field solution of the magnet matrix and the magnetic flux densities sensed by the Hall-effect sensors. Specifications of the Hall-effect sensor for a constant 2-mA current are presented in Table I. Each Hall-effect sensor has two orthogonal axes and measures the magnetic flux density in two independent perpendicular axes. The periodic magnetic flux density is then converted to a voltage signal, and based on the voltage variation and the fundamental wave number of the magnet matrix, the displacement of the platen is determined. A single Hall-effect sensor cannot detect the unique position of the platen because there are two equal magnitude points in a one-pitch sinusoidal magnetic flux density, since it exhibits symmetry and periodicity. Therefore, two Hall-effect sensors collaborate to measure one-axis motion. Moreover, the phase difference between the two Hall-effect sensors is used to determine the direction of motion.

TABLE I
SPECIFICATIONS OF THE 2-D-VD-11SO TWO-AXIS HALL-EFFECT SENSOR

Specifications	Value
Input resistance	2.2 kΩ
Output resistance	8.5 kΩ
Offset voltage	±3 mV
Sensitivity	400 mV/T
Resolution	2 μT
Magnetic sensitive volume	0.25 × 0.25 × 0.20 mm^3

A collaborative working approach was used in [13] to take advantage of linearity and low sensing noise in the sensitive intervals. One of the two adjacent sensors (the set of sensors A and B or the set of sensors A and C) is always located in one of the sensitive intervals, where the gradient of magnetic flux density is large with respect to its position. Since we use the sensitive intervals, sensor switching is required at every quarter pitch. This sensor switching takes place repeatedly as the platen moves over multiple pitches. Using this principle, the rotation about the z-axis can also be determined.

At this point there is no way to have any external sensor verification done on the stage to ensure that the remaining dynamics are due to stage motion. Since one of the key objectives of this research is to demonstrate the planar multivariable control of the positioner with inexpensive two-axis Hall-effect sensors while optimizing the signal to obtain a 1.5-μm position resolution. However, in the previous research paper [21], the Hall-effect sensor signal was calibrated against a laser interferometer. It was demonstrated that the distortions or errors can be compensated for with a 2-D lookup table since this error mostly originated from the nonideality of the magnet-matrix construction and was repeatable.

III. MULTIVARIABLE CONTROLLER DESIGN

A. Integrator Augmented LQ Design

An LQ controller guarantees a phase margin of at least 60° and possesses good robustness properties [22]. Furthermore, in an LQ design, some states can be intentionally penalized in the weighting matrix to achieve a desired dynamic performance. Therefore an LQ is suitable for the horizontal and vertical motion control. However, there are two main drawbacks for an LQ to be used in a servo mechanism. One is that as a regulator, an original form of an LQ cannot track a nonzero

reference input. The other is that there will be a steady-state error due to the nonexistence of integrators in an LQ design. In order to make the LQ operational for our system, we derive the tracking-error dynamics of the system to design an integrator-augmented LQ. The errors are defined as follows:

$$\Delta x = x - x^* \tag{8}$$

$$\Delta y = y - y^* \tag{9}$$

$$\Delta u = u - u^* \tag{10}$$

where x, y, and u are the state, output, and input vectors of the state-space model in the horizontal mode, which is represented in (11), and x^*, y^*, and u^* are the corresponding steady-state vectors, respectively

$$\begin{aligned} \dot{x} &= Ax + Bu \\ y &= Cx. \end{aligned} \tag{11}$$

The A, B, and C matrices are the corresponding state, input, and output matrices in the horizontal mode, respectively.

Taking the derivative of (8), we obtain the following error dynamics:

$$\Delta \dot{x} = \dot{x} - \dot{x}^* = A\Delta x + B\Delta u \tag{12}$$

$$\Delta y = C(x - x^*) = C\Delta x. \tag{13}$$

Next we augment integrators to the system to eliminate the steady-state error. The state-space model of the augmented system is presented as follows:

$$\begin{bmatrix} \Delta \dot{x}_p \\ \dot{z}_p \end{bmatrix} = \begin{bmatrix} A_p & 0 \\ C_p & 0 \end{bmatrix} \begin{bmatrix} \Delta x_p \\ z_p \end{bmatrix} + \begin{bmatrix} B_p \\ 0 \end{bmatrix} \Delta u_p \tag{14}$$

$$\Delta y_p = \begin{bmatrix} C_p & 0 \end{bmatrix} \begin{bmatrix} \Delta x_p \\ z_p \end{bmatrix} \tag{15}$$

where z_p are the integrator states.

As a result, the augmented system now has nine states altogether in the horizontal mode. Since all the nine states are available, an LQ can be designed for the system based on the augmented system (14) and (15). In an LQ design, the Q_{hor} and R_{hor} are constant weighting matrices corresponding to the horizontal mode, which are to be designed to penalize some state variables (or inputs) more than others to meet dynamic requirements. In this case, to eliminate the steady-state error effectively, we penalize the effect of the integrators heavily and the displacement states much more than the velocity states for better positioning performance. R_{hor} was set as a 3×3 identity matrix and Q_{hor} was designed as follows:

$$Q_{\text{hor}} = \text{diag}\left([\, 10^4 \;\; 10^4 \;\; 10^4 \;\; 10^8 \;\; 10^8 \;\; 10^8 \;\; 10 \;\; 10 \;\; 10 \,]\right). \tag{16}$$

The corresponding gain matrix K_{hor} was calculated to be

$$K_{\text{hor}} = \begin{bmatrix} -160.2 & 253.9 & -92 & -3523 & 6372 & -3183 & -3.46 & 4.74 & -1.18 \\ 158.3 & 264.7 & 88.2 & 3464 & 6629 & 3045 & 3.44 & 4.95 & 1.13 \\ 359.3 & -1.88 & -71.7 & 7949 & -59.5 & -2595 & 7.73 & -0.02 & -0.84 \end{bmatrix}. \tag{17}$$

For the vertical mode, the same LQ methodology described previously of adding integrators to the state-space model is used. In this case we have the Q_{ver} and R_{ver} constant weighting matrices corresponding to the vertical mode. Again to eliminate the steady-state error effectively, the integrator states were penalized heavily, then the displacement states were penalized more than the velocity states for better positioning performance. R_{ver} was set as a 3×3 identity matrix and Q_{ver} was designed as follows:

$$Q_{\text{ver}} = \text{diag}\left([\, 10^4 \;\; 10^4 \;\; 10^4 \;\; 10^9 \;\; 10^9 \;\; 10^9 \;\; 10^2 \;\; 10^2 \;\; 10^2 \,]\right). \tag{18}$$

The corresponding gain matrix K_{ver} was calculated to be

$$K_{\text{ver}} = \begin{bmatrix} 405.5 & -40.9 & 53.2 & 13869 & -2672 & 4109 & 6.1 & -0.9 & 1.4 \\ 442.5 & -40.5 & -49.1 & 15130 & -2633 & -3954 & 6.7 & -0.9 & -1.3 \\ 480 & 69.1 & 2.4 & 16407 & 4837 & 89.8 & 7.3 & 1.63 & 0.03 \end{bmatrix}. \tag{19}$$

B. State Estimator

The integrator-augmented LQ design relies on the presence of the complete state measurements. However, neither the laser distance sensors nor the Hall-effect sensors can directly provide the full states to the controller. The LQG control methodology is the combination of a Kalman filter and an LQ control law [23]. In order to get the full states, an observer is needed to estimate the missing states and optimize the known states. A method of combining discrete-Kalman ($\mathcal{H}_2$) and minimax ($\mathcal{H}_\infty$) filtering has been proposed in [14]. Kalman filtering is an optimal estimation method which minimizes the variance of the estimation error and assumes that the noise inputs have known statistical properties, which makes this filter lack robustness from the errors of the assumed noise statistics [14]. Unfortunately, the assumption that the statistical properties of the noise are known limits the application of the Kalman filter. The minimax filter aims to minimize the magnitude of the maximum singular value of the transfer function from the noise to the estimation error. In other words, it tries to minimize the worst possible estimated values. If the Kalman filter assumes too much, the minimax filter approach assumes too little, which motivates the interest in combining these two filters into a hybrid $\mathcal{H}_2/\mathcal{H}_\infty$ filter and see if it can provide the best of both filters.

Let us design the hybrid filter that will provide optimal displacement measurements as well as the estimates of the linear and angular velocities. The states of the hybrid filter are defined as

$$x_k = \begin{bmatrix} z_k \\ \dot{z}_k \\ \ddot{z}_k \end{bmatrix}, \qquad \text{for } z_k = \begin{bmatrix} x & y & \varphi & z & \theta & \psi \end{bmatrix}^T. \tag{20}$$

For continuous time, the dynamic model and measurement (estimated) model are

$$\begin{aligned} \dot{x}(t) &= \begin{bmatrix} \dot{z}(t) \\ \ddot{z}(t) \\ \dddot{z}(t) \end{bmatrix} = \begin{bmatrix} 0 & I_{6\times 6} & 0 \\ 0 & 0 & I_{6\times 6} \\ 0 & 0 & 0 \end{bmatrix} \begin{Bmatrix} z(t) \\ \dot{z}(t) \\ \ddot{z}(t) \end{Bmatrix} + \begin{bmatrix} 0 \\ 0 \\ I_{6\times 6} \end{bmatrix} w(t) \\ \tilde{y}(t) &= \hat{z}(t) + v(t) = \begin{bmatrix} I_{6\times 6} & 0 & 0 \end{bmatrix} x(t) + v(t). \end{aligned} \tag{21}$$

The inputs to the hybrid filter are the displacement data calculated from the Hall-effect sensors' outputs, v is a 6×1 vector and is the noise from the system. The tilde ($\tilde{}$) represents the estimates of the measured states of the hybrid filter

$$\tilde{y}(t) = \begin{bmatrix} \tilde{x} & \tilde{y} & \tilde{\varphi} & \tilde{z} & \tilde{\theta} & \tilde{\psi} \end{bmatrix}^T. \tag{22}$$

The relationships between position, velocity, and acceleration are modeled exactly without any modeling error. Note that the process noise w is a 6×1 vector which has the same unit as the jerk and does not depend on the modeling error. The constant-acceleration assumption is merely for a simple modeling purpose. In discrete time, the model becomes the following:

$$\begin{aligned} x_{k+1} &= \begin{bmatrix} I_{6\times6} & (t_{k+1}-t_k)I_{6\times6} & \frac{1}{2}(t_{k+1}-t_k)^2 I_{6\times6} \\ 0 & I_{6\times6} & (t_{k+1}-t_k)I_{6\times6} \\ 0 & 0 & I_{6\times6} \end{bmatrix} x_k \\ &\quad + \begin{bmatrix} \frac{1}{6}(t_{k+1}-t_k)^3 I_{6\times6} \\ \frac{1}{2}(t_{k+1}-t_k)^2 I_{6\times6} \\ (t_{k+1}-t_k)I_{6\times6} \end{bmatrix} w_k \\ &= \Phi x_k + \Upsilon w_k \\ \tilde{y}_k &= \begin{bmatrix} I_{6\times6} & 0 & 0 \end{bmatrix} x_k + v_k = H x_k + v_k \end{aligned} \tag{23}$$

where $(t_{k+1}-t_k)$ is the integration step size, which is constant for simulation and real-time control.

The estimator structure for the hybrid filter in [14] is of the form

$$\hat{x}^+ = \hat{x}^- + K[\tilde{y} - H\hat{x}^-] \tag{24}$$

where K is the hybrid filter gain. This hybrid filter uses a weighted combination of the steady-state Kalman and the steady-state minimax filter gains in the estimator, so the hybrid filter gain is defined as

$$K = d \cdot K_{\text{ss}}^K + (1-d) \cdot K_{\text{ss}}^\infty \tag{25}$$

where d is the relative weight given to K_{ss}^K which is the steady-state Kalman filter gain, and K_{ss}^∞ is the steady-state minimax filter gain. This relative weight ranges from 0 to 1 and must be chosen so as to ensure stability because a convex combination of two stable estimators is not necessarily stable. The discrete kalman filter (DKF) is presented in [24]. The vector v, the noise from the system, is assumed to be zero-mean Gaussian noise $v(t) \sim N(0, R_k)$, where R_k is the error covariance matrix of the system noise v, which is defined in [21] as

$$\begin{aligned} R_k &= (H_k^T W H_k)^{-1} \\ &= \text{diag}\left([\,10^{-6}\ 10^{-6}\ 10^{-6}\ 10^{-6}\ 10^{-6}\ 10^{-6}\,]\right). \end{aligned} \tag{26}$$

Further, w is assumed to be a zero-mean Gaussian process $w(t) \sim N(0, Q_k)$, where Q_k is the error covariance matrix of the process noise w, which acts on the acceleration. Q_k is chosen to be a positive constant diagonal matrix

$$Q_k = \text{diag}\left([\,10^3\ 10^3\ 10^5\ 10^2\ 10^2\ 10^2\,]\right) \tag{27}$$

where an assumption is made that v and w are uncorrelated, and the values of R_k and Q_k were chosen by the designer. Selecting the bounds of the process and system noises became the parameters to tune the DKF. The approach for selecting the values of each matrix was used by noticing that the system noise matrix R_k will be the same for all of the six axes, so a value was selected based on the experiments that would lead to acceptable results. The filter dynamics is related to the values of the matrix Q_k. Based on the experiments, it was noticed that smaller values of Q_k can filter out the noise effectively. However, it causes slow convergence with small bandwidth, which might lead to instability. Larger values of Q_k have high speed of convergence and a higher overshoot, and they cannot filter out noise as well. There is a design tradeoff, where large Q_k causes a faster response, but smaller values of Q_k are desired because they filter the noise, and the bandwidth of the filter needs to be faster than the controller, while effectively filtering out the noise. The bandwidth of the DKF was set at 85 Hz in x and y, 110 Hz in the rotation around z, and 65 Hz for z and the rotations around x and y. For the parameters of Q_k and R_k described previously, the steady-state DKF gain matrix K_{ss}^K turned out to be

$$K_{\text{ss}}^K = \begin{bmatrix} 0.0531 & 0 & 0 & 0 & 0 & 0 \\ 0 & 0.0531 & 0 & 0 & 0 & 0 \\ 0 & 0 & 0.1566 & 0 & 0 & 0 \\ 0 & 0 & 0 & 0.0364 & 0 & 0 \\ 0 & 0 & 0 & 0 & 0.0364 & 0 \\ 0 & 0 & 0 & 0 & 0 & 0.0364 \\ 1.390 & 0 & 0 & 0 & 0 & 0 \\ 0 & 1.390 & 0 & 0 & 0 & 0 \\ 0 & 0 & 9.47 & 0 & 0 & 0 \\ 0 & 0 & 0 & 0.752 & 0 & 0 \\ 0 & 0 & 0 & 0 & 0.752 & 0 \\ 0 & 0 & 0 & 0 & 0 & 0.752 \\ 37.42 & 0 & 0 & 0 & 0 & 0 \\ 0 & 37.42 & 0 & 0 & 0 & 0 \\ 0 & 0 & 351.3 & 0 & 0 & 0 \\ 0 & 0 & 0 & 12.05 & 0 & 0 \\ 0 & 0 & 0 & 0 & 12.05 & 0 \\ 0 & 0 & 0 & 0 & 0 & 12.05 \end{bmatrix}. \tag{28}$$

Using the same linear dynamic system as described above, the minimax filtering problem aims to minimize the maximum singular value of the transfer function from the noise to the estimation error [25]

$$J = \frac{\text{avg}\left\|x_k - \hat{x}_k\right\|_Q}{\text{avg}\left\|w_k\right\|_W + avg\left\|v_k\right\|_V} \tag{29}$$

where J is a measure of how good the estimator is. We want to find a state estimate that will minimize the worst possible effect that w and v have on the estimation error, where the averages are taken over all time samples k. Several minimax filtering formulations have been proposed in [26] and [27], the one considered here is the following. Find a filter gain K_{ss}^∞ such that the maximum singular value is less than γ, or $J < 1/\gamma$. This is a way of minimizing the worst-case estimation error, where γ is the constant which becomes the design parameter to tune this filter. We can find a state estimate so that the maximum value of J is always less than $\hat{x}$ regardless of the values of the noise terms w and v. This problem will have a solution for some values of γ but not for the values which are too small because the P matrix in the Riccatti equation will become singular, as seen in the minimax gain equation below. The minimax filtering solution that forces $J < 1/\gamma$ is given in [14] and [25], for which we do not need to worry about defining the matrices for w and v noises, which makes this the main advantage of such a filter. For $\gamma = 10$,

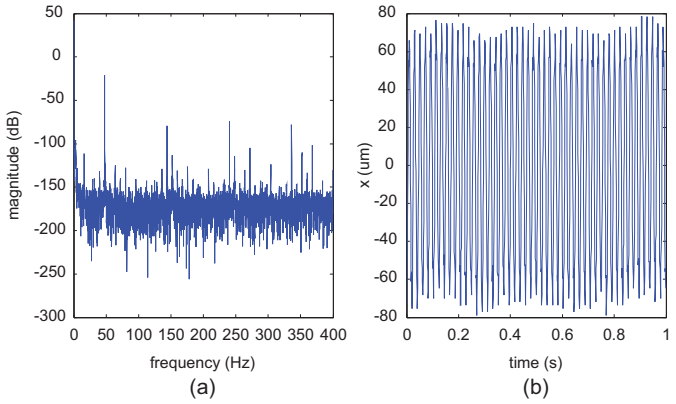

Fig. 3. (a) Measured spectrum of the output signal. (b) Time response.

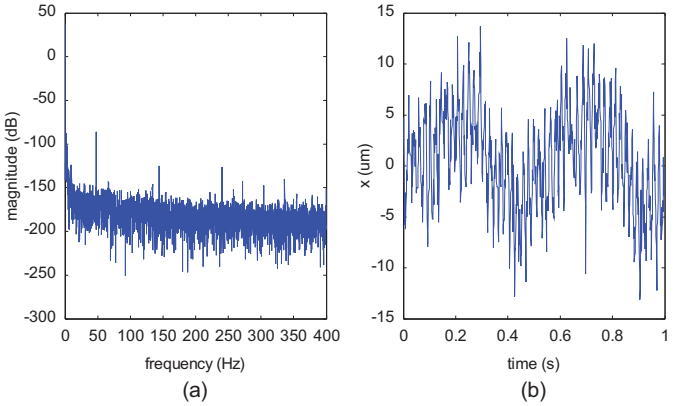

Fig. 4. (a) Measured spectrum of the output signal with hybrid filtering. (b) Time response.

the steady-state minimax filter gain matrix K_{ss}^{∞} turned out to be

$$K_{ss}^{\infty} = \begin{bmatrix} 0.637 & 0 & 0 & 0 & 0 & 0 \\ 0 & 0.637 & 0 & 0 & 0 & 0 \\ 0 & 0 & 0.637 & 0 & 0 & 0 \\ 0 & 0 & 0 & 0.637 & 0 & 0 \\ 0 & 0 & 0 & 0 & 0.637 & 0 \\ 0 & 0 & 0 & 0 & 0 & 0.637 \\ 0.0135 & 0 & 0 & 0 & 0 & 0 \\ 0 & 0.0135 & 0 & 0 & 0 & 0 \\ 0 & 0 & 0.0135 & 0 & 0 & 0 \\ 0 & 0 & 0 & 0.0135 & 0 & 0 \\ 0 & 0 & 0 & 0 & 0.0135 & 0 \\ 0 & 0 & 0 & 0 & 0 & 0.0135 \\ -0.8e{-}4 & 0 & 0 & 0 & 0 & 0 \\ 0 & -0.8e{-}4 & 0 & 0 & 0 & 0 \\ 0 & 0 & -0.8e{-}4 & 0 & 0 & 0 \\ 0 & 0 & 0 & -0.8e{-}4 & 0 & 0 \\ 0 & 0 & 0 & 0 & -0.8e{-}4 & 0 \\ 0 & 0 & 0 & 0 & 0 & -0.8e{-}4 \end{bmatrix}. \quad (30)$$

IV. Hall-Effect Sensor Signal Analysis

A. Analysis

In order to analyze the noise of the Hall-effect sensors, a fast Fourier transform (FFT) is performed for the planar MIMO system under the control law described in Section III. For these experiments, the controller makes the platen move to a specified coordinate in the x plane with the controller doing its best to stay put. For the first test, the LQ control law is applied without the hybrid filter being active. The results are displayed in Fig. 3. From the FFT one can see that there is a peak at 50 Hz of around -30 dB in magnitude. The response of the signal for 1 s is also included, and the peak-to-peak position noise is around 160 μm.

The next test applies the hybrid $\mathcal{H}_2/\mathcal{H}_\infty$ filter, making the controller to be an LQ with hybrid $\mathcal{H}_2/\mathcal{H}_\infty$ control. The results are displayed in Fig. 4. The peak-to-peak position noise of the signal has been reduced to 20 μm. From the FFT, the 50-Hz peak has been reduced to -60 dB in magnitude. For the experiments involving the hybrid filter being active, the relative weight of such filter d is 1, so the hybrid filter acts as a DKF.

The nature of the systematic 50-Hz noise was found to be purely electric, coming from the Hall-effect sensors. The Hall-effect sensors are manufactured by a company located in Europe, where the standard frequency of the electricity coming from the electrical outlet is 50 Hz [28]. Oscilloscope measurements confirmed that the 50-Hz peak noise comes from the Hall-effect sensors.

B. Second-Order Digital Notch Filter Design

The digital filter will essentially act as a "prefilter," because the data being read from the sensor will be filtered first by a digital second-order notch filter, and then will be further filtered by the DKF observer. The second-order notch digital filter will have the notch set at 50 Hz, eliminating the peak noise and leading to more precise results than those in Section III. The second-order notch filter is of the form [29]

$$H(j\omega) = \frac{-k\omega^2 + \omega_0^2}{-\omega^2 + 2\zeta\omega_0(j\omega) + \omega_0^2} \quad (31)$$

where $s = j\omega$ was substituted, ζ is the damping ratio of the filter set to be 0.5, k is related to the attenuation at high frequencies, and ω_0 is the constant for which we are solving for. In order to get a notch, the numerator of the transfer function has to be zero at a fixed frequency ω_{notch}. This would make the magnitude of the transfer function go to zero at such frequency. The equation for the numerator of the transfer function is

$$-k\omega_{\text{notch}}^2 + \omega_0^2 = 0 \quad (32)$$

where we solve for ω_0, since ω_{notch} becomes the frequency in which we want the notch to occur, which was shown to be at 50 Hz. However we still have not solved for k, which relates to the attenuation of the signal at the higher frequencies. Due to the harmonics from the 50-Hz biased noise, attenuation is necessary at higher frequencies. A -20-dB attenuation is desired at high frequencies, which means that -20 dB $= 20\log(k)$, this makes $k = 0.1$. The attenuation cannot be set too low because the stability of the system can be degraded.

Substituting $k = 0.1$ and the notch frequency into (32) gives

$$\omega_0 = 2\pi \cdot 50\sqrt{0.1} \text{ rad/s}. \quad (33)$$

Substituting the value of k and ω_0 into (31) gives us the final form of the second-order analog notch filter. Transforming the analog filter to its digital form gives

$$H(z) = \frac{0.09318 - 0.1733z^{-1} + 0.09318z^{-2}}{1 - 1.792z^{-1} + 0.8047z^{-2}}. \quad (34)$$

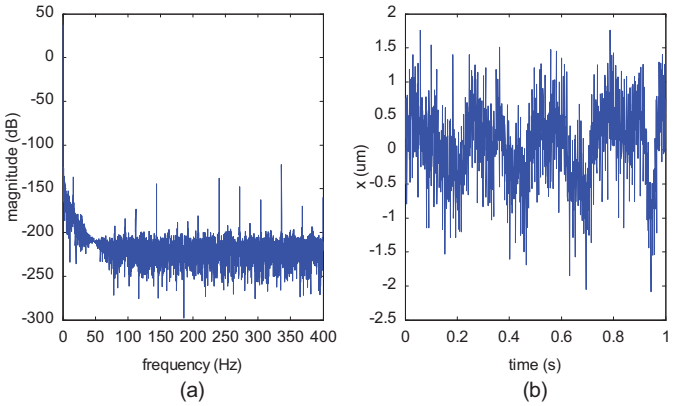

Fig. 5. (a) Measured spectrum of the output signal with notch filtering and without hybrid filtering. (b) Time response.

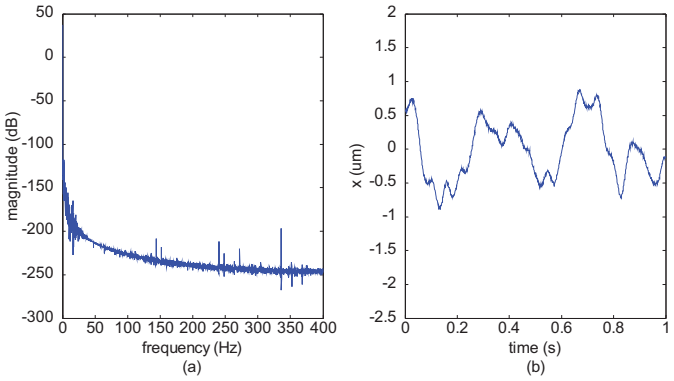

Fig. 6. (a) Measured spectrum of the output signal with notch filtering combined with hybrid filtering. (b) Time response.

The aforementioned digital notch filter is implemented without the DKF filter making the controller a regular LQ controller, since the notch filter does not estimate the velocities of the states. An FFT is performed on the signal response, and the signal response is plotted for a second, as shown in Fig. 5. The peak-to-peak noise of the signal has been enhanced to 4 μm. From the FFT, one can see that the peak at 50 Hz has been essentially eliminated.

Finally both filters are applied together with the digital notch filter acting as a prefilter while the DKF acts as the observer. As seen in Fig. 6, the peak-to-peak position noise has been enhanced to 1.5 μm. The peak at 50 Hz has been eliminated, thus proving the effectiveness of having the digital second-order notch filter act as a prefilter on the incoming sensor signal and then have the hybrid filter further reduce the noise of the signal. The digital notch filter combined with the hybrid filter provides the best results with optimal position control for the planar motion.

V. Experimental Results

This section presents the comparisons between our results and those in [8], as well the experimental results obtained for various hybrid filter weights with and without the digital notch filter being active. For the recursive hybrid filter, various hybrid $\mathcal{H}_2/\mathcal{H}_\infty$ filter weights are used in order to see how it affects the signal response of the Hall-effect sensors and to

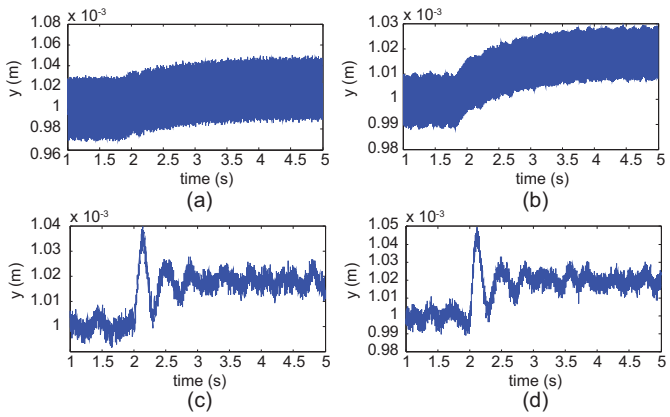

Fig. 7. 20-μm step responses for hybrid filter weights of (a) $d = 0$, (b) $d = 0.3$, (c) $d = 0.8$, and (d) $d = 1$ without digital notch filtering.

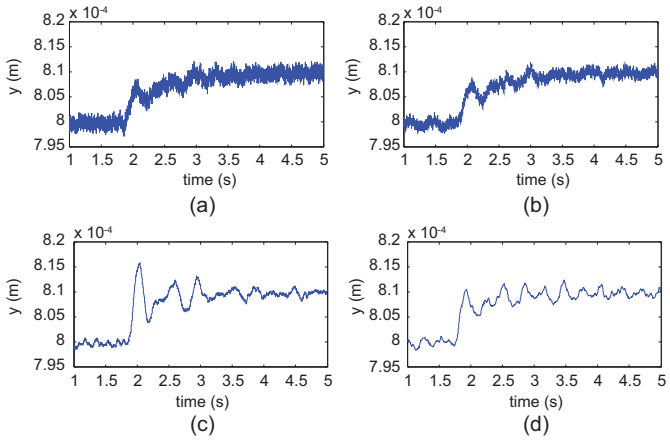

Fig. 8. 10-μm step responses for hybrid filter weights of (a) $d = 0$, (b) $d = 0.3$, (c) $d = 0.8$, and (d) $d = 1$ with digital notch filtering.

see whether a certain value of the hybrid $\mathcal{H}_2/\mathcal{H}_\infty$ filter weight leads to a higher positioning resolution. The comparisons are done with and without the digital notch filter being active. The results are shown in Figs. 7 and 8. All of the experiments were done while the system was given a step input in the y-direction.

The results show that, without the digital notch filtering, a combination of the hybrid $\mathcal{H}_2/\mathcal{H}_\infty$ filter gives better resolution than the DKF or the minimax filter. For this scenario the optimal hybrid $\mathcal{H}_2/\mathcal{H}_\infty$ filter weight is $d = 0.8$, for which a 16-μm peak to peak position noise was achieved, however, when the notch digital filter is implemented along with the hybrid $\mathcal{H}_2/\mathcal{H}_\infty$ filter, the DKF provides the best optimal estimates for the position in the planar motion with a 1.5-μm peak-to-peak position noise.

The DKF provides better estimates when the digital notch filter is implemented because the notch filter eliminates the main source of the narrow-band noise at 50 Hz, and it attenuates the harmonics of such noise at high frequencies. By eliminating the main source of the nonrandom noise, the DKF can provide optimal estimates because the main assumption for the DKF implementation is that the noise has to be random with a Gaussian distribution. Therefore whenever the

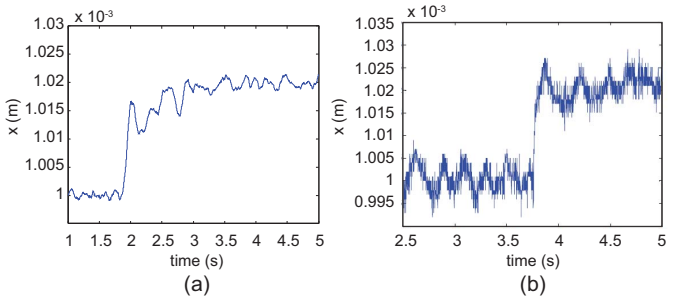

Fig. 9. 20-μm step response in x comparing (a) our results and (b) Yu's [8].

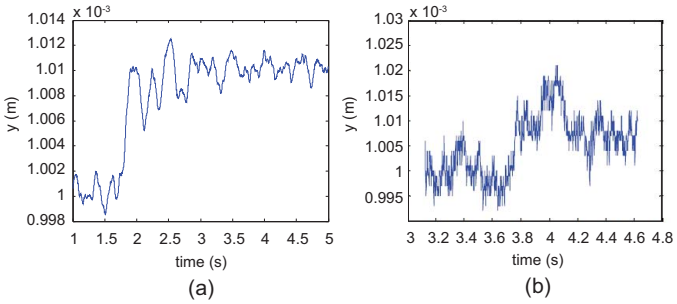

Fig. 10. 10-μm step response in y comparing (a) our results and (b) Yu's [8].

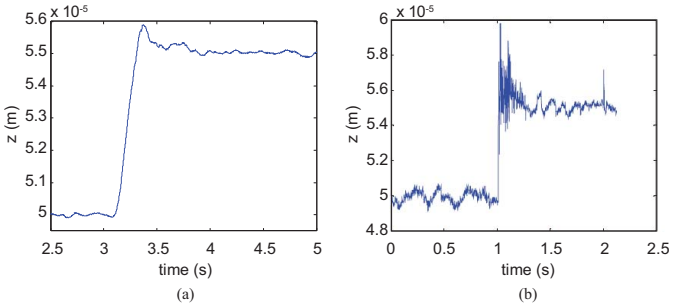

Fig. 11. 5-μm step response in z comparing (a) our results and (b) Yu's [8].

digital notch filter is not implemented, the 50-Hz noise and its harmonics exhibit a significant magnitude. This prevents the DKF from being an optimal state estimator, which is the reason why the hybrid $\mathcal{H}_2/\mathcal{H}_\infty$ filter with a weight of 0.8 gives better estimates.

Moreover, as designers of the filter, we wished to significantly improve the DKF performance of the hybrid filter, which relates to the signal resolution. In order to do this, however, we had to compromise the $\mathcal{H}_\infty$ performance. In addition to resolution, performance in terms of robustness, peak error, and dynamic response of the system were of interest in the practical design. In terms of the resolution without digital filtering, $d = 0.8$ was the best choice. However, when digital filtering was implemented, $d = 1$ gave the best resolution, and the signal seems more sensitive to noise/disturbance effects than that in the $d = 0.8$ plot. The filter is more robust in such case, but at the same time the dynamic response is also worse.

The step responses used in the comparisons are taken from [8] and [13]. In both of them, Yu used lead-lag controllers

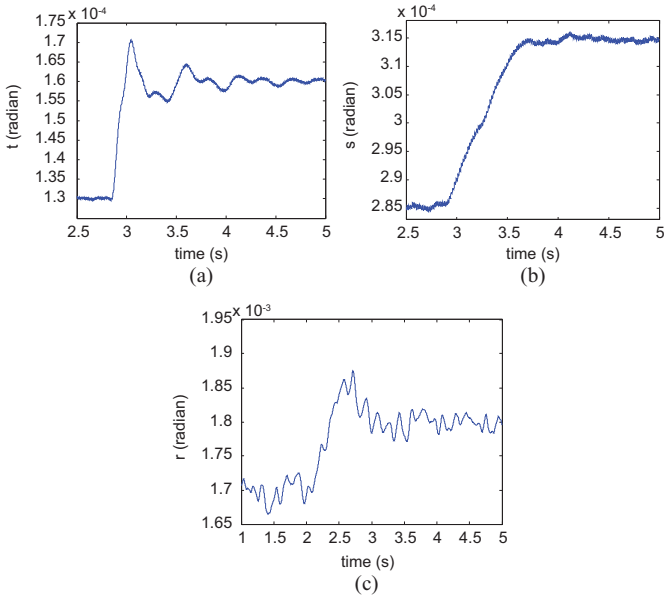

Fig. 12. Closed-loop responses. (a) 30-μrad step response in θ. (b) 30-μrad step response in ψ. (c) 100-μrad step response in ϕ.

to control each axis individually and a DKF to obtain better estimates in the planar mode. Our results in the planar mode have digital notch filter implemented and the LQ controller with a hybrid $\mathcal{H}_2/\mathcal{H}_\infty$ estimator acting as a DKF whereas the vertical mode uses only the LQ controller with a hybrid $\mathcal{H}_2/\mathcal{H}_\infty$ estimator ($d = 1.0$). Fig. 9 shows a comparison for a 20-μm step in x, and Figs. 10 and 11 show a comparison for a 10-μm step in y and a 5-μm step in z, respectively. The closed-loop responses in the other 3-DOF motions, which are the rotations about the x-, y-, and z-axes, are shown in Fig. 12, for 30-μrad, 30-μrad, and 100-μrad step commands, respectively.

Yu's step responses demonstrated a 14-μm resolution with an 8-μm rms position noise in the planar mode and for the vertical mode, a 0.8-μm resolution with a 0.5-μm rms position noise. Our results show a 1.5-μm resolution with a 0.545-μm rms position noise in the planar mode, and for the vertical mode, a 110-nm resolution with a 49.3-nm rms position noise. In the case of the vertical mode, there were small noise components at 50 Hz originated from the Hall-effect sensor line, which could be eliminated with the notch filter. Since the magnitude of the noise was small, however, it was unnecessary. Even the advantage of using the hybrid filter weight of $d = 0.8$ to using the DKF is insignificant due to the small magnitude of the noise.

A suggestion for a "scenario" where the hybrid filter outperforms the combination of the DKF and the digital notch filter would be an application where there is poor noise knowledge of the system and such noise is significant in magnitude. For instance, an aerospace application, where the process noise is unknown or there can be low carrier-to-noise ratios for the measurement noise. In such applications there is always a biased process noise that is constantly affecting the readings such as gusts of wind, for which the frequency is variant. In our precision-positioning application, it is unlikely that there

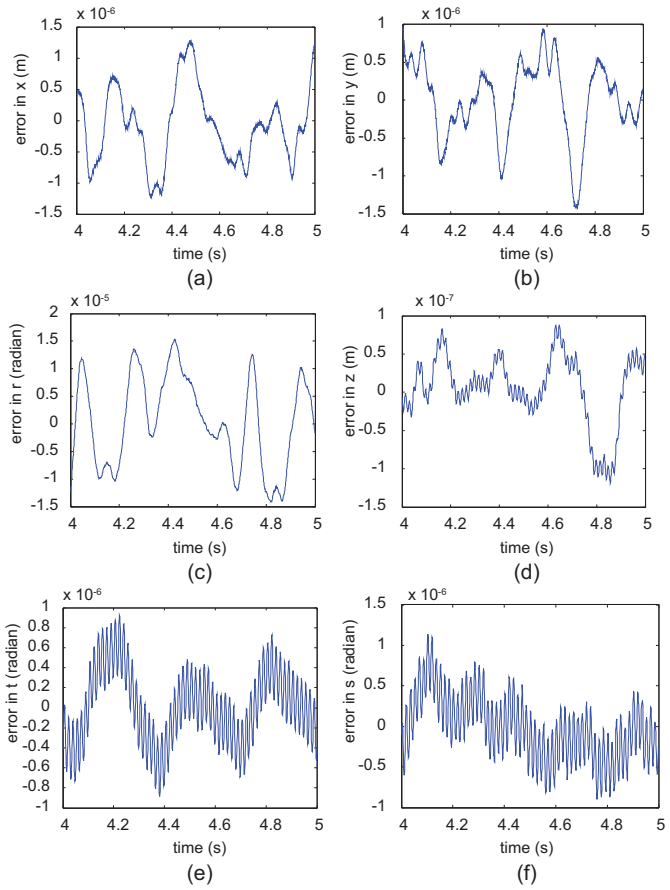

Fig. 13. Tracking error for the step responses in (a) x, (b) y, (c) ϕ, (d) z, (e) θ, and (f) ψ.

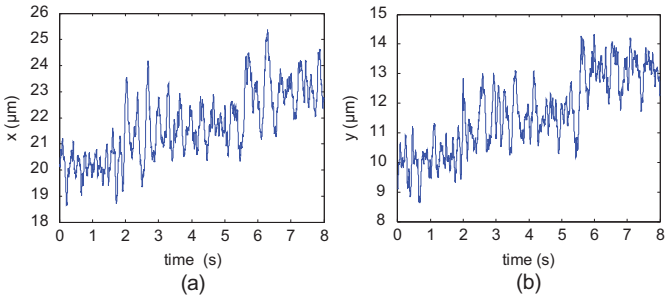

Fig. 14. Consecutive 1.5-μm step responses in (a) x and (b) y.

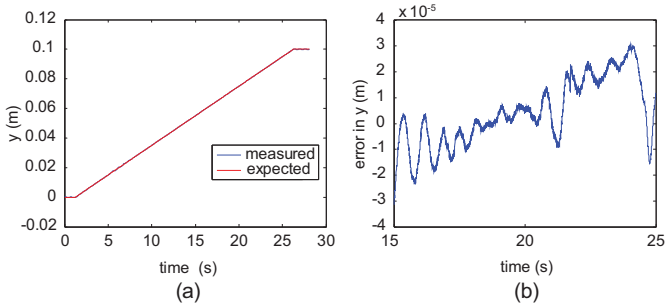

Fig. 15. (a) 100-mm long-range motion in y. (b) Position error over 10-s duration.

is large process noise in a closed-door environment where the vibrations from the ground are minimal, especially since the stage is sitting on top of an optical table.

A better position resolution was obtained in our results for both the planar and the vertical modes. However, our results have a slower rise time and settling time, but at the same time they also have smaller overshoot magnitudes. The slower time response of the dynamic system is due to the tradeoff of having a low system bandwidth, while the small overshoot is both an effect of the bandwidth of the filters and the controllers. The bandwidths of the multivariable controllers are set at a range of 9–30 Hz for the planar mode, and 30–60 Hz for the vertical mode. This is the frequency above which the system output does not track the system input, if the latter is a sinusoid. The bandwidths were set this low, because otherwise it will put a severe restriction in the design of the observer, and an observer with such a high bandwidth cannot attenuate the noise well. However, the aim of this paper is to have a reliable positioner for step-and-repeat motions, and for this application a sinusoidal motion at a frequency of more than 10 Hz will be unnecessary.

Fig. 13(a)–(c) shows the tracking error plots of the step responses for the horizontal mode shown in Figs. 11 and 12. From these plots, we can see that the tracking errors in the x-, y-, and ϕ-axes are less than 1.5 μm and 15 μrad, respectively. The steady-state errors are calculated over the span of 1 s, and they came out to be 176.2 nm in x, 135.3 nm in y, and 1.24 μrad in ϕ. Thus the steady-state errors are less than 2%. Fig. 13(d)–(f) presents the tracking error plots for the step responses of the vertical mode shown in Figs. 11 and 12. These plots show that the tracking errors in the z-axis are less than 110 nm and those in the θ- and ψ-axes are less than 1 μ and 1.5 μrad, respectively. The steady-state errors are calculated over the span of 1 s, which came out to be 14.8 nm in z, 91.9 nrad in θ, and 35.6 nrad in ψ. The steady-state errors in the vertical mode are all less than 0.4%, which indicates that the integrator-augmented LQG controller successfully controlled the system in the vertical as well as horizontal mode.

Key limiting factors in position resolution include the Hall-effect sensors' sensitivity, the NanoGage laser distance sensors' sensitivity, misalignments in the magnet matrix, and disturbances transmitted through the umbilical cables attached to the moving platen, and acoustic noises from the three aerostatic bearings for levitation. However, in the horizontal mode, the errors are bigger than those in the vertical mode because the laser distance sensors used in the vertical mode have a higher resolution compared to the Hall-effect sensors in the horizontal mode even when the high-magnitude electrical noise is filtered.

To demonstrate the positioning resolution of the platen in the planar mode, consecutive steps of 1.5-μm are presented in Fig. 14 in both the x- and y-axes. The steps took place at $t = 2$ and 5.5 s for both figures. Fig. 15 shows a 100-mm long-range motion in y and the position error over 10-s duration. When the platen suddenly stops, the error increases but it eventually reaches the steady state. The error in tracking the signal is directly related to the scanning velocity of the platen, 4 mm/s in this case. It is true that the noise measurement varies at

different positions in the magnet matrix mainly because the matrix is not perfectly symmetrical and there may be some small misalignments in it.

VI. Conclusion

This paper presented the successful implementation of two multivariable controllers using an LQ controller with a hybrid $\mathcal{H}_2/\mathcal{H}_\infty$ estimator acting as the observer for a 6-DOF positioner with Linux-based real-time control. This novel positioning stage has only a 1.52-kg single moving part and is based on a patented concentrated-field magnet matrix. An analysis was done for the Hall-effect sensor signals, and based on the results, a digital second-order notch filter was designed and implemented to eliminate the biased noise and achieve better positioning resolution in the planar motion.

The detailed procedure of designing the multivariable controllers for the positioning stage was presented in this paper. Since the sensors in the horizontal and vertical modes cannot measure the velocity states, an LQ controller with a hybrid $\mathcal{H}_2/\mathcal{H}_\infty$ estimator was designed. An integrator-augmented LQ was designed and implemented in both modes, while a six-axis recursive discrete hybrid $\mathcal{H}_2/\mathcal{H}_\infty$ filter was implemented to obtain a full-state feedback by estimating the velocity estimates and optimizing the position states. The hybrid $\mathcal{H}_2/\mathcal{H}_\infty$ filter was also implemented instead of a conventional Kalman filter in an effort to obtain a better position resolution and to see if it provides any advantage over pure Kalman or minimax filters.

The step responses demonstrated the integrator-augmented LQ controller's good tracking performance and high-resolution positioning capabilities. Several comparisons were made among various hybrid $\mathcal{H}_2/\mathcal{H}_\infty$ filter weights with and without the digital notch filter being active. It was shown that when the digital filter is active, the hybrid $\mathcal{H}_2/\mathcal{H}_\infty$ filter acting as the DKF gives the best positioning resolution, however, when the digital filter is inactive, a hybrid $\mathcal{H}_2/\mathcal{H}_\infty$ filter weight of $d = 0.8$ gives the best positioning resolution. This is because the digital filter eliminates the main source of the narrow-band noise at 50-Hz thus making the DKF effective. Whenever the digital filter is inactive, however this noise made the DKF not as effective as the hybrid $\mathcal{H}_2/\mathcal{H}_\infty$ filter.

Experimental results were presented for all 6 DOFs to display the performance of the controller and the digital filter design. The positioner was able to achieve a position resolution of 1.5 μm with a position noise of 0.545 μm rms in the xy plane, and for the vertical mode, the positioner achieved a position resolution of 110 nm with a position noise of 49.3 nm. This is about a factor-of-10 improvement from the previous results.

References

[1] R. A. de Callafon and P. M. J. Van den Hof, "Multivariable feedback relevant system identification of a wafer stepper system," *IEEE Trans. Control Syst. Technol.*, vol. 9, no. 2, pp. 381–382, Mar. 2001.

[2] M. Quirk and J. Serda, *Semiconductor Manufacturing Technology*. Upper Saddle River, NJ: Prentice-Hall, 2001.

[3] J. Cao, Y. Zhu, J. Wang, W. Yin, and G. Duan, "Analysis and comparison of two-dimensional permanent-magnet arrays for planar motor," *IEEE Trans. Magn.*, vol. 40, no. 6, pp. 3490–3494, Nov. 2004.

[4] H.-S. Cho, C.-H. Im, and H.-K. Jung, "Magnetic field analysis of 2-D permanent magnet array for planar motor," *IEEE Trans. Magn.*, vol. 37, no. 5, pp. 3762–3766, Sep. 2001.

[5] B. A. Sawyer, "Magnetic positioning device," U.S. Patent 3 376 578, Apr. 2, 1968.

[6] *Northern Magnetics Linear Motor Technology Manual*, Northern Magnetics Inc., Santa Clarita, CA, 1998.

[7] J. Pan, N. C. Cheung, and J. Yang, "Structure and characteristics of closed-loop two-dimensional surface motors - a literature survey," in *Proc. IEEE 5th Int. Conf. Power Electron. Drive Syst.*, Nov. 2003, pp. 236–241.

[8] H. Yu, "Design and control of a compact 6-degree-of-freedom precision positioner with Linux-based real-time control," Ph.D. dissertation, Dept. Mech. Eng., Texas A&M Univ., College Station, Aug. 2009.

[9] D. L. Trumper, W.-J. Kim, and M. E. Williams, "Magnetic arrays," U.S. Patent 5 631 618, May 20, 1997.

[10] W.-J. Kim, "High-precision planar magnetic levitation," Ph.D. dissertation, Dept. Electr. Eng. Comput. Sci., Massachusetts Inst. Technology, Cambridge, Jun. 1997.

[11] W.-J. Kim, N. Bhat, and T. Hu, "Integrated multidimensional positioner for precision manufacturing," *J. Eng. Manuf., Proc. Inst. Mech. Eng., B*, vol. 218, no. 4, pp. 431–442, Apr. 2004.

[12] T. Hu and W.-J. Kim, "Extended range six-DOF high-precision positioner for wafer processing," *IEEE/ASME Trans. Mechatron.*, vol. 11, no. 6, pp. 682–689, Dec. 2006.

[13] H. Yu and W.-J. Kim, "A compact Hall-effect-sensing 6-DOF precision positioner," *IEEE/ASME Trans. Mechatron.*, vol. 15, no. 6, pp. 982–985, Dec. 2010.

[14] D. Simon and H. El-Sheried, "Hybrid Kalman/minimax filtering in phase-locked loops," *Control Eng. Pract.*, vol. 4, no. 5, pp. 615–623, May 1996.

[15] D.-J. Jwo and R.-J. Chen, "Mixed H_2/H_∞ filtering approach for GPS/INS navigation systems," in *Proc. IEEE Int. Conf. Recent Adv. Space Technol.*, Nov. 2003, pp. 409–414.

[16] X. Z. Liu, G. C. Verghese, J. H. Lang, and M. K. Önder, "Generalizing the Blondel-Park transformation of electrical machines: Necessary and sufficient conditions," *IEEE Trans. Circuits Syst.*, vol. 36, no. 8, pp. 1058–1067, Aug. 1989.

[17] R. H. Park, "Two-reaction theory of synchronous machines generalized method of analysis-part I," *Trans. Amer. Inst. Electr. Eng.*, vol. 48, no. 3, pp. 716–730, Jul. 1929.

[18] D. L. Trumper, W.-J. Kim, and M. E. Williams, "Design and analysis framework for linear permanent-magnet machines," *IEEE Trans. Ind. Appl.*, vol. 32, no. 2, pp. 371–379, Mar.–Apr. 1996.

[19] A. E. Fitzgerald, C. Kingsley, Jr., and S. D. Umans, *Electric Machinery*, 5th ed. New York: McGraw-Hill, 1990.

[20] J. C. Silva-Rivas, "Control and optimization of a compact 6-degree-of-freedom precision positioner using combined digital filtering techniques," Dept. Mech. Eng., M.S. thesis, Texas A&M Univ., College Station, Dec. 2011.

[21] Y. Kawato and W.-J. Kim, "Multi-degree-of-freedom precision position sensing and motion control using two-axis Hall-effect sensors," *Trans. ASME, J. Dyn. Syst., Meas., Control*, vol. 128, no. 4, pp. 980–988, Dec. 2006.

[22] C. Zhang and M. Fu, "A revisit to the gain and phase margins of linear quadratic regulators," *IEEE Trans. Autom. Control*, vol. 41, no. 10, pp. 1527–1530, Oct. 1996.

[23] S. Skogestad and I. Postlethwaite, *Multivariable Feedback Control Analysis and Design*. New York: Wiley, 1996.

[24] J. L. Crassidis and J. L. Junkins, *Optimal Estimation of Dynamic Systems*, 2nd ed. Boca Raton, FL: Chapman & Hall, 2004.

[25] D. Simon, "From here to infinity," *Embedded Syst. Program.*, vol. 14, no. 11, pp. 20–32, Oct. 2001.

[26] U. Shaked and Y. Theodor, "H_∞ optimal estimation: A tutorial," in *Proc. 31st IEEE Conf. Decision Control*, Tucson, AZ, Dec. 1992, pp. 2278–2286.

[27] K. Zhou and P. Khargonekar, "An algebraic Ricatti equation approach to H_∞ optimization," *Syst. Control Lett.*, vol. 11, no. 1, pp. 167–172, Aug. 1988.

[28] *Sentron AG*. (2011) [Online]. Available: http://www.sentron.nl

[29] J. G. Proakis and D. G. Manolakis, *Digital Signal Processing*, 3rd ed. Upper Saddle River, NJ: Prentice-Hall, 1996.

Jose Christian Silva-Rivas received the B.Sc. degree in mechanical engineering from The University of Texas at Austin, Austin, in 2009, and the M.Sc. degree from the Department of Mechanical Engineering, Texas A&M University, College Station, in 2011, where he is currently pursuing the Ph.D. degree in mechanical engineering.

His current research interests include real-time control system design, digital signal processing, and optimal estimation of dynamic systems.

Won-jong Kim (S'89–M'97–SM'03) received the B.S. (*summa cum laude*) and M.S. degrees in control and instrumentation engineering from Seoul National University, Seoul, Korea, in 1989 and 1991, respectively, and the Ph.D. degree in electrical engineering and computer science from the Massachusetts Institute of Technology, Cambridge, in 1997.

He has been with the Department of Mechanical Engineering, Texas A&M University, College Station, since 2000, where he is currently an Associate Professor. His current research interests include analysis, design, and real-time control of mechatronic systems, networked control systems, and nanoscale engineering and technology. He holds three U.S. patents on precision positioning systems.

Dr. Kim was a recipient of the Gulf Oil/Thomas A. Dietz Career Development Professorship II for period 2007-2010. He is a fellow of the American Society of Mechanical Engineers and a member of Pi Tau Sigma. He is the Technical Editor of the IEEE/ASME TRANSACTIONS ON MECHATRONICS, the *ASME Journal of Dynamic Systems, Measurement and Control, International Journal of Control, Automation, and Systems*, and the *Asian Journal of Control*.